5-6-2019

Examination of Proverse Yaw in Bell-Shaped Spanload Aircraft

Jonathan Richter
Washington University in St. Louis

Kevin Hainline
Washington University in St. Louis

Ramesh K. Agarwal
Washington University in St. Louis

Examination of Proverse Yaw in Bell-Shaped Spanload Aircraft

MEMS 400: Independent Study Final Report

Jonathan Richter
McKelvey School of Engineering
Washington University in St. Louis

Research Advisors: Mr. Kevin Hainline & Dr. Ramesh K. Agarwal

Abstract

Recent developments in the bell-shaped spanload have shown the existence of proverse yaw control power via induced thrust at the wingtips. With no need for vertical control surfaces, new types of aircraft designs are possible. Via the use of traditional roll and proverse yaw control power, a lateral directional control space can be created for flying wings where no sweep is required for lateral directional stability and control. These straight tapered flying wings have increased efficiency and performance compared to traditional aircraft. In order to maintain stability and control, straight tapered flying wings require adequate proverse yaw control power. This paper investigated the connection between aircraft geometry and proverse yaw control power while applying the bell spanload.

A straight tapered flying wing Biomimetic Aircraft was used for the initial aircraft geometry. By varying taper ratio, wing chord, wing length, twist distribution, and outboard wing control surface (OWCS) size, several relationships between aircraft geometry and proverse yaw control power are determined. Proverse yaw control power is a function of the change in lift over a region of upwash as well as the change in localized downwash. As the OWCS area increases due to larger chord lengths, proverse yaw control power increases. Additionally, increasing the region of upwash via a longer wingspan or twist distribution leads to improved proverse yaw control power. However, increasing the span fraction of the OWCS does not necessarily result in increased proverse yaw control power as it is tied to localized downwash. Varying the lift distribution due to an OWCS deflection can positively affect this downwash decreasing proverse yaw control power. The Biomimetic Aircraft with 10% more span and 10% more twist at the wingtips has 16 times more proverse yaw control power than the original Biomimetic Vehicle. With this increase in proverse yaw control power, straight tapered flying wings are controllable through all necessary flight regimes.

Nomenclature

CL	= Coefficient of roll moment with respect to control surface deflection
CN	= Coefficient of yaw moment with respect to control surface deflection
C_L/Cl	= Lift Coefficient
c	= chord
b	= span
L	= Lift
MAC	= Mean Aerodynamic Center
IWCS/Inneron	= Inboard Wing Control Surface
OWCS/Outeron	= Outboard Wing Control Surface
Biom	= Biomimetic Blended-Wing-Body UAV
DP	= Differential Pressure

Introduction

Lacking tails, flying wings generally offer an increase in efficiency when compared to conventional aircraft. However, traditional flying wings must be swept back to increase both pitch and yaw stability. Increased induced drag due to span-wise flow is the cost of this required stability, and it lowers the net performance of the aircraft. This can be shown through Kuchemann's modification to Helmbold's equation where performance decreases by roughly the cosine of the sweep angle [1, p.474]. As a result, some high-performance aircraft, such as sailplanes, continue to use traditional wing and tail designs. Bell-shaped spanload aircraft can utilize proverse yaw control power in combination with traditional roll control power (both roll and adverse yaw) to create a lateral directional control space [2]. Given sufficient lateral and directional stability, an aircraft, neutrally stable in pitch, can be flown via the use of a closed loop flight controller eliminating the need for sweep increasing aircraft efficiency [2]. Maximizing proverse yaw control power and maintaining the optimal bell-shaped spanload is critical to the success of straight tapered flying wing design.

In 2016, researchers at the NASA Armstrong Flight Research Center under the supervision of Albion Bowers demonstrated the increased efficiency and stability of bell-shaped spanload aircraft. Compared to the traditional elliptical lift distribution which only has downwash along the span, the bell-spanload has both regions of downwash and upwash [3]. The point at which the downwash begins to transition to upwash is defined as the vortex shed line as mid span vortices occur at that point rather than the wingtips. The transition point between downwash and upwash is labeled in the Fig. 1 below.

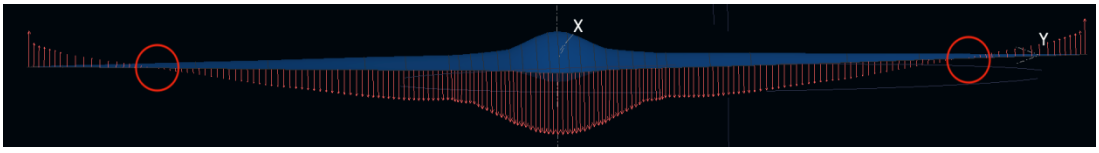

Fig. 1 Downwash Distribution from Bell Shaped Spanload (Processed in XFLR5).

Through the development of the "Prandtl-d" swept flying wing glider, Bowers successfully measured and linked proverse yaw to upwash and induced thrust created at the wingtips by the bell-shaped spanload [3]. This connection tied together decades of research.

Beginning in 1921, Ludwig Prandtl published *Applications of Modern Hydrodynamics to Aeronautics* and proposed, through his lifting line theory, the elliptical lift distribution as the

solution to the minimum induced drag case [4]. Continuing in 1933 with his *On Wings with Minimum Induced Drag*, Prandtl recognized that his original work was incomplete, and by replacing the span constraint with a root-bending moment constraint, the bell-shaped spanload became the optimal lift distribution for minimizing induced drag [5]. Compared to the elliptical distribution, the bell spanload had a 22% larger span and an 11% increase in efficiency [3]. The Prandtl solution was separately confirmed by R. T. Jones at NACA [6]. Several variations on the bell-spanload arise from variations on the constraints, such as accounting for viscous drag and wing weight (see Klein and others) [7][8][9][10][11]. Building on the research of Bowers, Hainline in 2017 examined an offshoot of the bell-shaped spanload: proverse yaw. Re-examining the original constraints on tailless flying wings, Hainline established a lateral-directional control space (Fig. 2) through the use of inboard control surfaces (IWCS/innerons) relying on adverse yaw and roll and outboard control surfaces (OWCS/outerons) relying on proverse yaw [2]. With an established lateral-directional control space, all sweep was eliminated from the flying wing sacrificing some pitch stability but significantly increasing its efficiency and performance [2]. This aircraft, the Original Biomimetic Flight Vehicle (Fig. 3a), became the starting point of this study.

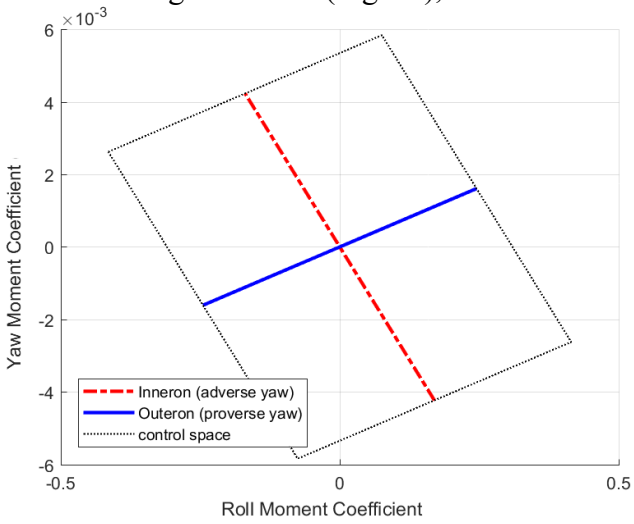

Fig. 2 Lateral Directional Control Space [2].

Methods of Data Analysis

All data collected in this experiment was from OpenVSP's viscous lattice panel method which applies viscous analysis to thin airfoil theory. OpenVSP is an open source parametric geometry modeling software developed by J. R. Gloudemans at NASA Ames and later released under the NASA open source agreement (NOSA) version 1.3. OpenVSP's wing geometry editor facilitates easy changes in airfoil choice, taper ratio, and washout. OpenVSP does not enforce mirroring across the x-z body plane and thus facilitated simulating differential full moving wing deflections. Additionally, OpenVSP's breakdown of local lift over mean aerodynamic chord (MAC) allows for an in-depth analysis of lift on crucial sections of the wing. All data except otherwise noted was analyzed in MATLAB.

Proverse Yaw Analysis Studies

Seven different aircraft based off of the Original Biomimetic Flight Vehicle ("Original Biom" for short) were analyzed for their proverse yaw characteristics (see Fig. 3a). All aircraft, unless otherwise noted, used a combination of geometric and aerodynamic angle of attack to fit the bell-spanload originally defined by Prandtl and confirmed by Bowers (Eq. 1 and Fig. 4) [3]. Each aircraft explored the effects of geometry on proverse yaw control power. The Biom with Full

Moving OWCS coined the “FM Biom” (Fig. 3b) replaced the OWCS on the Original Biom with Full Moving (FM) OWCS. All following aircraft also utilized FM OWCS, and thus the FM Biom became the baseline of the study. The Biom with 20% Less Taper (Fig. 3c) examined the effect of taper on proverse yaw control power. The Biom with 30% Smaller Wingtips (Fig. 3d) reduced all chords except the root chord by 30%. Similarly, The Biom with 30% Larger Wingtips (Fig. 3e) increased all chords but the root chord by 30%. The Biom with 20% Larger OWCS (Fig. 3f) increased the OWCS chord sections by 20%. The Biom with 10% Larger Span increased the span of the aircraft by 10% from 2.0m to 2.1m (Fig. 3g).

In addition to the seven aircraft planforms, variations on the bell-spanload were studied on the FM Biom, the Biom with 20% Larger OWCS, and the Biom with 10% Larger Span. Also the span fraction at which the OWCS began was varied from 71.2% through its original placement of 76.0% to 90.4% on the FM Biom.

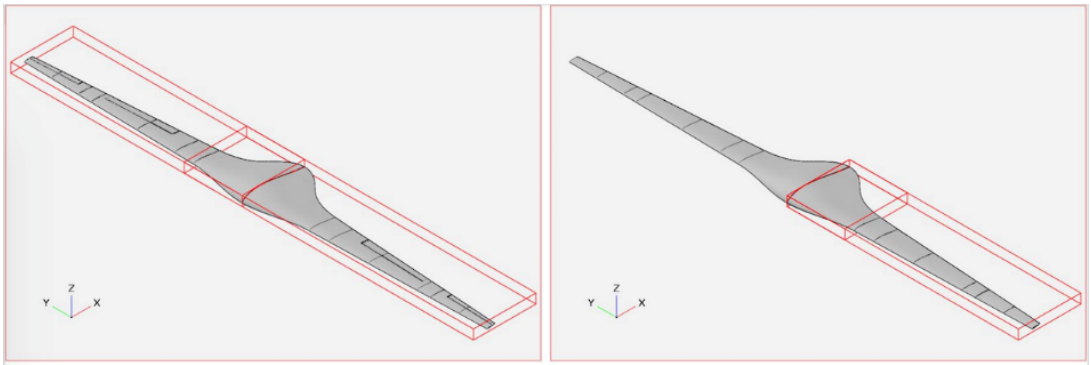

(a) Original Biomimetic Flight Vehicle

(b) Biom with Full Moving OWCS

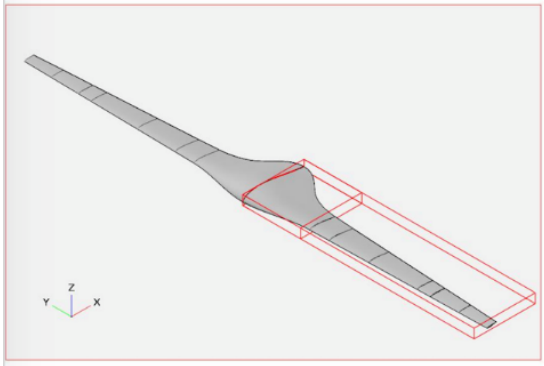

(c) Biom with 20% Less Taper

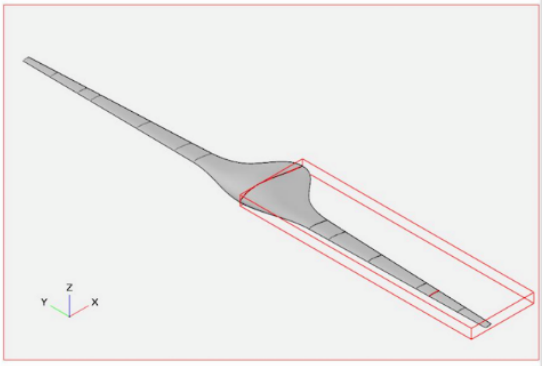

(d) Biom with 30% Smaller Wingtips

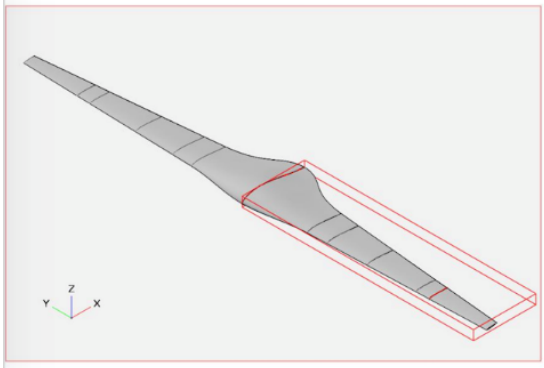

(e) Biom with 30% Larger Wingtips

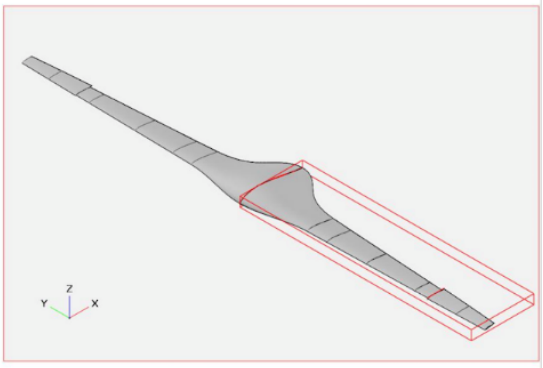

(f) Biom with 20% Larger OWCS

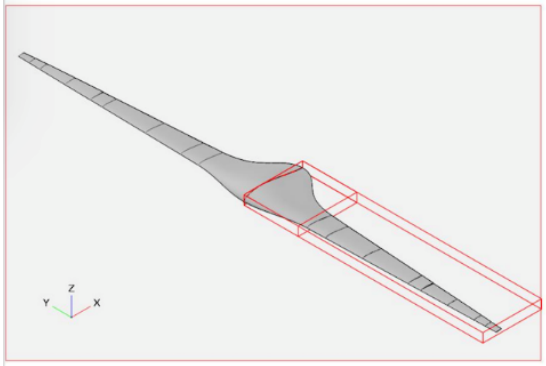

(g) Biom 10% Larger Span

Fig. 3 Aircraft Studied.

The bell shaped spanload described by Prandtl [4] and Bowers [3] is as follows:

$$L(y) = L|_{y=0}(1 - y^2)^{\frac{3}{2}} \quad (1)$$

where L(y) is the local lift, $L|_{y=0}$ is the lift at the center of the half-span (b/2), and y is the location along the half-span ranging from -b/2 to b/2. This equation is used in conjunction with local lift data from OpenVSP to generate the bell shaped spanload for the seven aircraft studied. If the initial lift distribution did not match the bell spanload; the geometric and or aerodynamic angle of attack were varied to achieve the bell spanload.

Figure four below displays the end results of editing aerodynamic and geometric angles of attack on the Original Biom to achieve the bell shaped spanload. Around y = 0, there was error in the OpenVSP panel solver, and as a result, a sharp discontinuity in lift exists. However, this error is negligible when compared to the overall lift distribution.

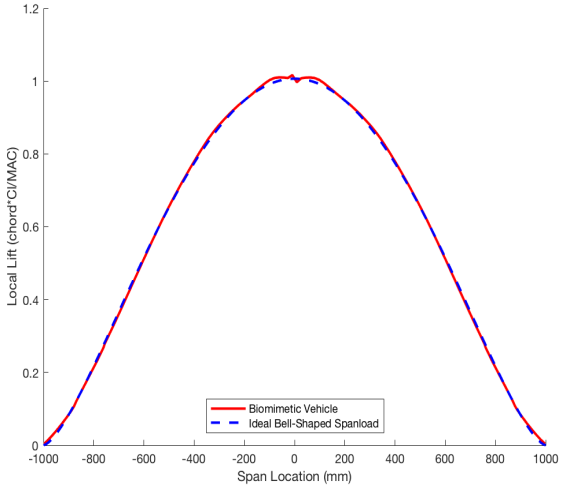

Fig. 4 Bell Shaped Spanload.

Table one below details the aircraft geometry for the FM Biom. Section six has a span length of one millimeter since it is used to deflect the FM wingtip. The Original Biom is extremely similar to the FM Biom with only two differences. The aircraft does not have section six and instead the one millimeter is distributed equally over sections seven and eight. Also, rather than being full moving, the Original Biom's OWCS ran from 0.8b/2 to 1.0b/2 and represented a uniform chord section of 0.35c.

Table 1 Wing Geometry Definition: Biom with Full Moving OWCS.

Section [#]	y [mm]	chord [mm]	twist [deg]	camber [%]	thickness [%]
0	0.00	270.00	0.00	3.0	15.0
1	250	113.75	2.83	1.5	9.0
2	333	105.035	0.25	1.0	9.0
3	500	87.50	-0.85	1.0	9.0
4	704	66.08	-2.00	0.0	9.0
5	760	60.20	-0.85	0.0	9.0
6	761	60.095	0.00	0.0	9.0
7	880.50	47.55	-2.30	0.0	9.0
8	1000	35.00	-2.10	0.0	9.0

The Biom with FM OWCS with -2 degrees of twist has an additional -2 degrees of twist evenly distributed over sections seven and eight of its wing. Figure five below details the lift distribution of this aircraft.

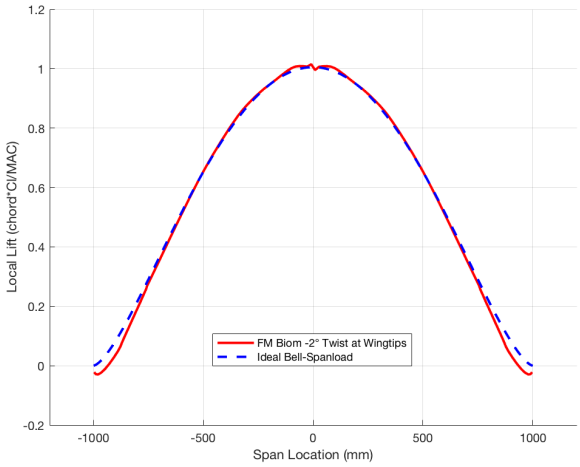

Fig. 5 Lift Distribution of the Full Moving Biom with -2° Twist in the Wingtips.

Table two provides details of aircraft geometry for the Biom with 20% Larger OWCS. The chord section increases at section six as the OWCS no longer follows the linear taper ratio.

Table 2 Wing Geometry Definition: Biom with 20% Larger OWCS.

Section [#]	y [mm]	chord [mm]	twist [deg]	camber [%]	thickness [%]
0	0.00	270.00	0.00	3.0	15.0
1	250	113.75	3.90	1.5	9.0
2	333	105.035	0.16	1.0	9.0
3	500	87.50	-1.00	1.0	9.0
4	704	66.08	-2.30	0.0	9.0
5	760	60.20	-1.15	0.0	9.0
6	761	72.11	0.00	0.0	9.0
7	880.50	57.06	-2.75	0.0	9.0
8	1000	42.00	-2.53	0.0	9.0

Figure six below displays the lift distribution of the Biom with 20% Larger OWCS with an additional -2 degrees of twist evenly distributed on sections seven and eight.

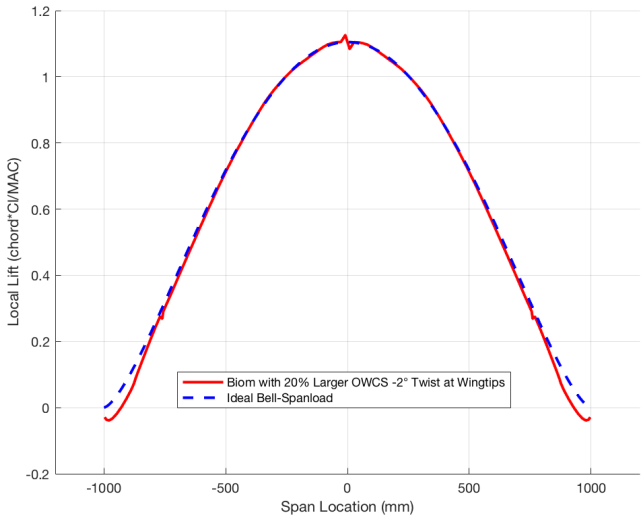

Fig. 6 Lift Distribution of the Biom with 20% Larger OWCS with -2° Twist at the Wingtips.

Table three below provides details of the geometry of the Biom with 10% Larger Span. The taper ratio for the outer wing section was kept constant, so the resultant tip chord was smaller than the original tip chord. The baseline model is the same as the FM Biom except for the addition of two sections to account for the increased length.

Table 3 Wing Geometry Definition: Biom with 10% Larger Span.

Section [#]	y [mm]	chord [mm]	twist [deg]	camber [%]	thickness [%]
9	1050	29.75	0.00	0.0	9.0
10	1100	24.50	0.00	0.0	9.0

Below in Fig. 7 is the lift distribution for the Biom with 10% Larger Span as well as two additional variants of the Biom with 10% Larger Span. One variant had an additional -2 degrees of twist in the outer two panels and one variant had an additional -10 degrees of twist in the outer two panels. Note that there is an increase in localized lift near the wingtip in the -2 and -10 degree cases. This error in OpenVSP's panel software likely lowers the amount of proverse yaw control power generated by both cases.

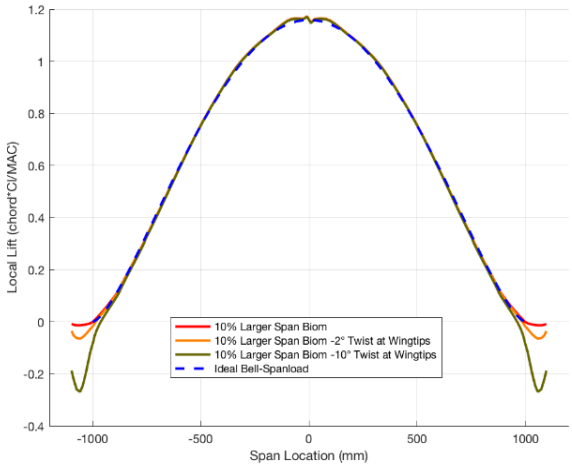

Fig. 7 Lift Distribution Biom with 10% Larger Span and Various Amounts of Twist at the Wingtips.

Results

Before all other aircraft were tested for their proverse yaw control power, the Original Biom was tested through a range of deflection angles. This data was used to determine the best angle at which to test deflections. Since OpenVSP is a numerical panel solver, it predicted linear trends for both roll and yaw data as expected. Since linear analysis is most likely valid with small deflection angles, all aircraft control power deflections were measured at two degrees.

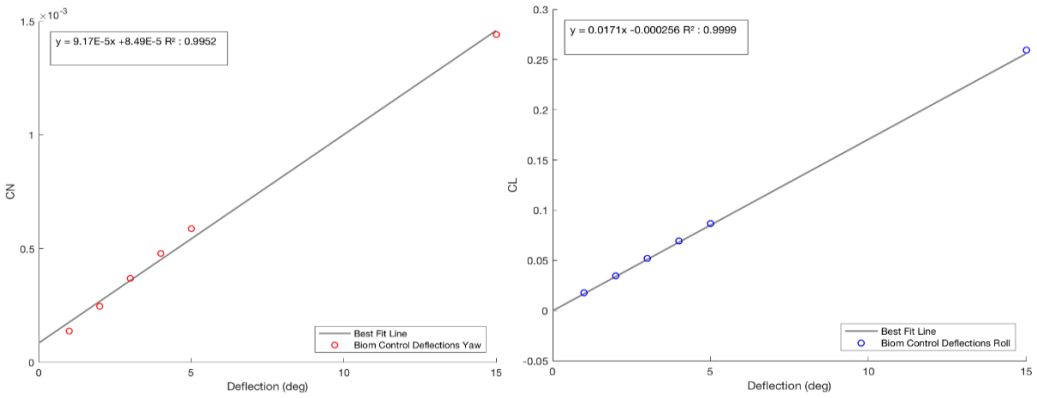

Fig. 8 (left) and Fig. 9 (right) Proverse Yaw and Roll Control Power Respectively.

Figure 10 below is a graph of roll control power vs. proverse yaw control power for all aircraft within the study. Compared to the Original Biom, every aircraft studied had a considerable increase in proverse yaw control power. Additionally, the aircraft modified with negative twist had an increase in yaw control power compared to their baseline models and no increase in roll control power. These results are valid as all proverse yaw control power data fell within the same order of magnitude as proverse yaw control power predicted and experimentally obtained by Bowers seen in Fig. 11 [3].

Figure 11 below is the plot of lift coefficient vs. proverse yaw control power performed by Bowers. Here, Bowers used Cnda (coefficient of yawing moment with respect to aileron deflection) instead of CN as his swept flying wings had only a single set of control surfaces responsible for creating the lateral-directional-pitch control space [3]. For the purposes of analysis, Cnda is equivalent to CN. Bowers plotted CN vs. Lift Coefficient since he obtained experimental data at various flight conditions. In the Biom studies, all aircraft were tested at cruise.

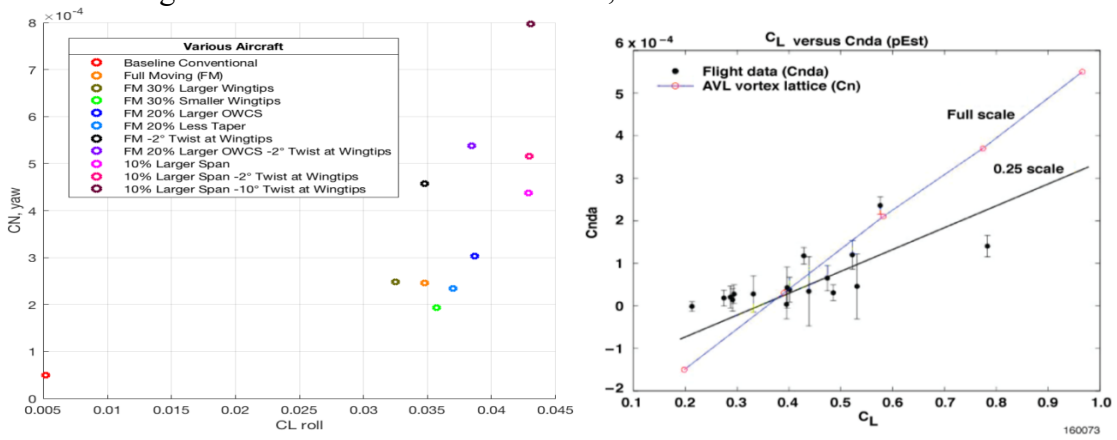

Fig. 10 (left) Roll vs. Yaw Control Power for Various Aircraft and Wing Twist Distributions.
Fig. 11 (right) C_N vs C_L from NASA Armstrong Flight Research Center [3].

Figure 12 below is the plot of roll control power vs. the yaw control power for different span fractions of the OWCS. The midspan vortex occurs at roughly 70%, so the first span fraction point was set just inboard of the vortex at 71.2% [3]. A local maximum for proverse yaw control power exists between 76.0% and 82.0% of the overall half-span.

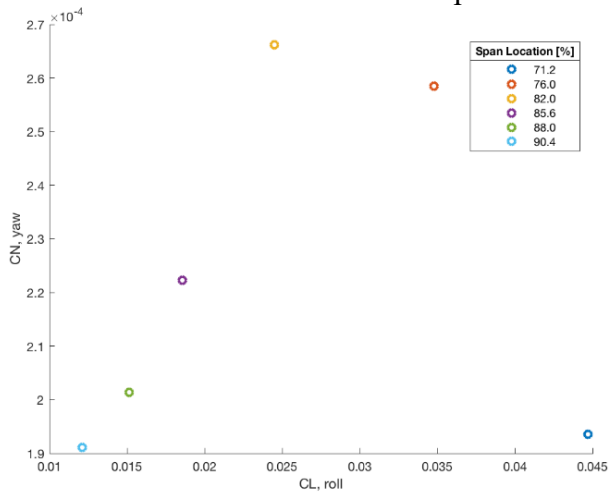

Fig. 12 Yaw vs. Roll Control Power with Various Span Fractions for OWCS.

Below in Fig. 13 is the local drag distribution plot for the Original Biom aircraft. This graph displays a positive deflection of the outeron and inneron on the right wing creating lift and a negative deflection of both surfaces on the left wing decreasing lift. The black vertical dashed lines signify the approximate locations of the outeron inner span fraction. Drag is created inboard of the positively deflected outeron and induced thrust exists just outboard of the positively deflected outeron. The sharp discontinuities in the drag plot are the result of insufficient panels on the aircraft. However, if more panels are added, then the solution does not converge. For the purposes of this study, the drag profile reveals important general characteristics of upwash. However, improved drag models are required for future research and more in depth examinations of induced thrust.

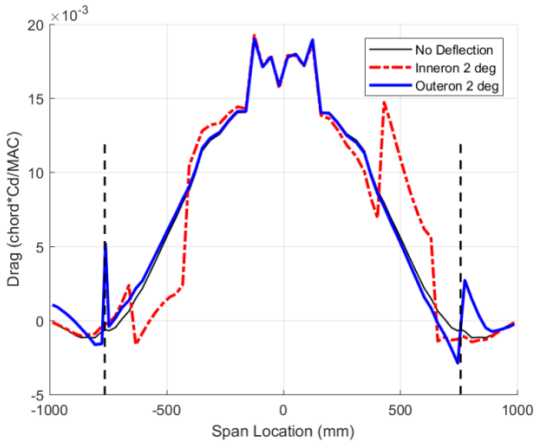

Fig. 13 Local Drag vs. Span.

Discussion

Several relationships between wing shape and proverse yaw were determined, but future research is required for a more complete understanding of proverse yaw's connection to aircraft geometry. Compared to the Original Biomimetic Vehicle, the author increased proverse yaw

control power by a factor of 16 from a C_N of $0.5*10^{-4}$ to a CN of $7.98*10^{-4}$ for the Biom with 10% Larger Span and -10 degrees of twist (Fig. 10).

Bower's 2016 paper links proverse yaw control power to upwash and induced thrust. He states that an increase in lift within the region of upwash (due to an OWCS or other control deflection) would lead to an increase of induced thrust and as a result, an increase in proverse yaw control power [3]. This would allow aircraft to perform coordinated turns without rudders.

This theory reliably predicts about half of the results shown in Fig. 10. The Biom with 20% Larger OWCS, and 10% Larger Span, all have increased levels of proverse yaw control power compared to the FM Biom and Original Biom. These aircraft create more lift within the upwash region with the same control deflection. Additionally, the aircraft with edited twist geometry also saw increased levels of proverse yaw control power as the vortex shed line likely shifted towards the root chord providing a larger region of upwash and as a result, more proverse yaw control power (Fig 10). The aircraft with increased twist had their proverse yaw control power increase with no increase in roll authority. This is logical as the increased upwash would tilt the lift vector slightly further forward leading to a larger induced thrust component. The roll component should decrease but given that roll authority is on the order of 10^{-2} and yaw authority is on 10^{-4}, any decrease in roll authority caused by the increased upwash is likely extremely marginal as the cosine of a very small angle is still approximately one.

However, the link between increased lift outside of the vortex shed line and proverse yaw control power breaks down in some circumstances. Specifically, it does not explain the results of the Biom with 30% Larger and Smaller Wingtips. One would expect the Biom with 30% Larger Wingtips to produce roughly 30% more proverse yaw control power compared to the FM Biom and the Biom with 30% Smaller Wingtips to produce roughly 30% less given the linear relationship between wing area and lift generation. The Biom with 30% Larger Wingtips produces a similar amount of proverse yaw control power as the FM Biom and the Biom with 30% Smaller Wingtips produces about 20% less proverse yaw control power (Fig. 10). This non-proportional relationship between the Biom with 30% Smaller and Larger Wingtips is not explained by Bower's published theory. Additionally, the Biom with 20% Less Taper should have more proverse yaw control power when compared to the FM Biom as more wing area is distributed within the region of upwash. Finally, applying the same upwash theory would conclude that the maximum amount of proverse yaw control power should occur when the OWCS encompasses the entire upwash region. This theory conflicts with data from Fig. 12 where there the local maximum for proverse yaw control power is between 76.0% and 82.0% of the half-span, and not at 71.2% which is just outside of the vortex shed line [3].

The data from the Biom with 30% Smaller Wingtips, 30% Larger Wingtips, and 20% Less Taper as well as the span fraction study suggests that the local effects of downwash influence proverse yaw control power. While further study is needed to directly determine the underlying factors contributing to proverse yaw on those aircraft configurations, a variation of Bower's published theory predicts the results of the span faction study. If one treats the OWCS as a lifting line horseshoe vortex filament, then deflecting the OWCS to create lift and induced thrust also creates increased downwash inboard of the OWCS span fraction and increased upwash outboard of the OWCS span fraction. When the OWCS spans the entire upwash region, deflecting the OWCS creates a strong local downwash over the entire former region of upwash essentially neutralizing the induced thrust. When the OWCS only encompasses the outer section of the upwash region, the upwash inboard the OWCS span fraction increases due to the upwash created from the OWCS deflection. The induced thrust inboard of the OWCS span fraction contributes to

proverse yaw control power. This explains the local maximum seen in Fig. 12, and also explains the region of induced thrust inboard of the outeron control surface deflection in Fig. 13. When determining proverse yaw control power, both change in lift over the upwash region (predicted by Bowers) [3] as well as the change in local downwash over the upwash region must be considered.[1]

Conclusion/Research Efforts in Progress

Proverse yaw control power is crucial for straight tapered flying wings, and by linking proverse yaw control power to the size of the OWCS, lift distribution, upwash, and the vortex shed line, straight tapered flying wings can be designed with ample directional stability. In this study, the author was able to increase the amount of proverse yaw control power by a factor of 16 which allows straight tapered flying wings to become a reality leading to significant increases in efficiency and performance.

To further develop relationships between proverse yaw control power and aircraft design, more research and data is required. Increasing the number of analyzed bell-shaped spanload aircraft configurations would allow for more quantitative relationships to be drawn between proverse yaw control power and aircraft geometry. With more data, an analytical solution for predicted proverse yaw control power may be possible. Also, future research should study the impact of increased proverse yaw control power on induced drag and attempt to determine a relationship between proverse yaw and induced drag. This connection could be crucial for maximizing proverse yaw control power while keeping induced drag within accepted limits.

To further validate this research, the author and Hainline plan to build a small-scale prototype Biomimetic Vehicle. Nearly identical to the FM Biom, the prototype Biom features full moving OWCS placed at roughly 80.0% of the overall span fraction for maximum proverse yaw control power and a thicker center section to accommodate an electric ducted motor and necessary flight hardware (Fig. 14).

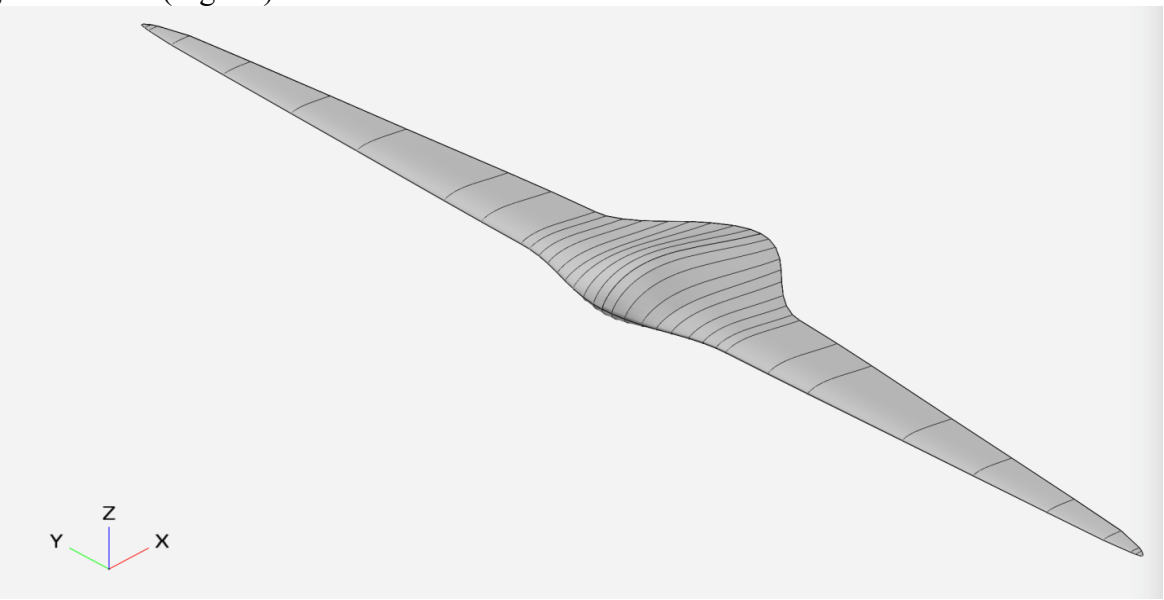

Fig. 14 2.2 Meter Biomimetic Prototype Vehicle.

[1] It is important to note that during a discussion with Bowers in January of 2019, the author and Kevin Hainline brought up this difference in his published theory and observed phenomena. Bowers claimed that the downwash spoilage was to be expected, but to this date he has not publicly clarified his theory.

Addendum to Research: Beta Detection Devices

After completing preliminary proverse yaw control analyses, the author was tasked with developing a beta probe that would measure the sideslip angle of the 2.2 Meter Biomimetic Prototype Vehicle. Despite the large increase in proverse yaw control power obtained from the study above, the Biom still has minimal yaw authority compared to other aircraft. Detecting aircraft drift in sideslip is crucial as any slippage must be immediately corrected before it falls outside of the lateral directional control space.

Traditionally, aircraft have utilized a variety of weathervane type designs as shown in Fig. 15 below to capture beta sideslip angle. When the aircraft begins to slip the freestream pushes against the side surface area of the vane and this deflection is measured by an electrical sensor [12].

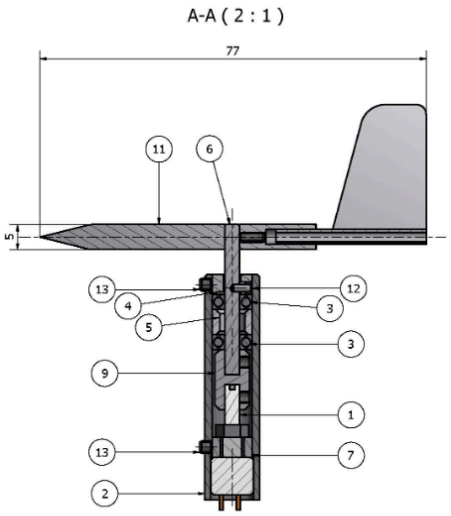

Fig. 15 Traditional Beta Vane Design [12].

However, the Biom was intended to have minimal side surface area and adding a beta vane would defeat this purpose. As a result, a secondary option was considered where a beta probe would be utilized. Generally packaged as a two in one beta and alpha probe, beta and alpha probes use a differential pressure sensor to detect sideslip and angle of attack from at least five different pressure taps [13]. Commercially available beta and alpha probes were too large, heavy, and expensive to use on this project, so the author began to design a simpler beta probe that would meet the Biom's necessary design requirements. Since most beta probes were developed for commercial sale, there is no publicly available data on beta probe design practices and no available wind tunnel data. To design the beta probe, the author relied on information used to design pitot tubes as their shape and size are similar to beta probes. However, even with pitot tubes, there was limited information on their design, wind tunnel testing, and manufacture.

Fundamentals of Aerodynamics 6th Edition by John Anderson provided an insightful technical discussion on pitot tube design. The design parameters discussed by Anderson were used to guide the construction of the Beta Probe and are shown in Fig. 16 below. To estimate the pressure differential between the two pressure taps on the probe, the Cp slope was linearized surrounding the head of the probe. This information was used to determine sensor selection.

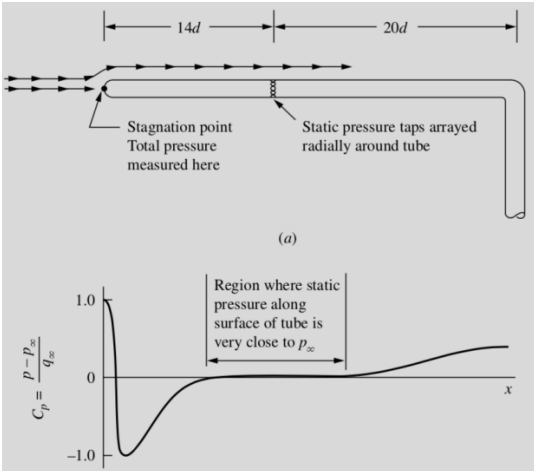

Fig. 16 Design Parameters and Pressure Distribution for Pitot Tubes [1, p. 231].

Design and Testing

The author worked with Peter Sharpe to make a Solidworks model of a preliminary beta probe design. Given the small size of the probe and the differential pressure holes, manufacturing was a major concern which weighed heavily on development. Despite lower tolerances, 3D printing was the best method as no traditional manufacturing method could produce the small vein like paths in the interior of the probe. Over the course of several months, the probe was repeatedly printed until the optimal print settings were determined. Below in Figs. 17 and 18 is the beta probe in Solidworks and the 3D printed version. To see a CAD drawing of the beta probe with more dimensions and views of the inner pressure vanes, see Appendix A.

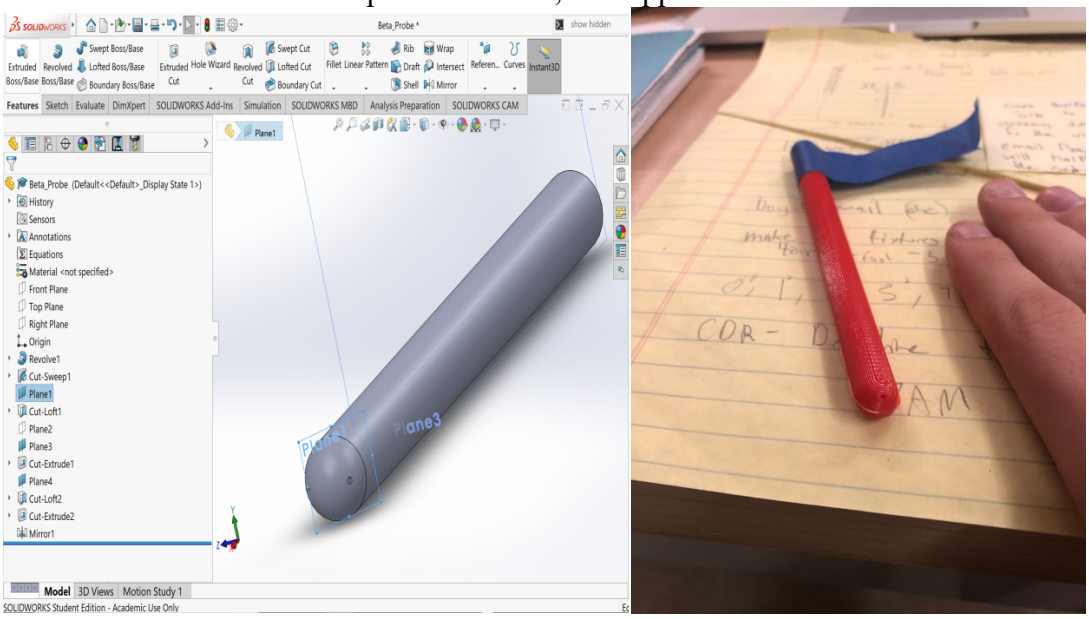

Fig. 17 (left) and 18 (right) The Beta Probe in Solidworks and the 3D printed Beta Probe.

A Sensirion SDP31 differential pressure sensor was selected to measure the pressure differential as its 16 bit precision and range of -500Pa to 500Pa included all possible pressure values and enough precision to differentiate between deflection angles [14]. Using an Arduino Uno, pressure data was read from the SDP31 via an I2C datalink. Once all devices were incorporated, the pressure sensor and beta probe were tested in a low speed wind tunnel between

0 and 24.1m/s at angles between zero and seven degrees. The wind tunnel was current limited via an electrical breaker, and unable to achieve speeds higher than 24.1m/s. This prevented testing to occur over the entire flight envelope of 0 to 40 m/s. Future testing is needed to confirm if the beta probe operates in velocities above 24.1 m/s. Figures 19 and 20 below detail the wind tunnel setup and the electrical setup of the Arduino and SDP31 interface.

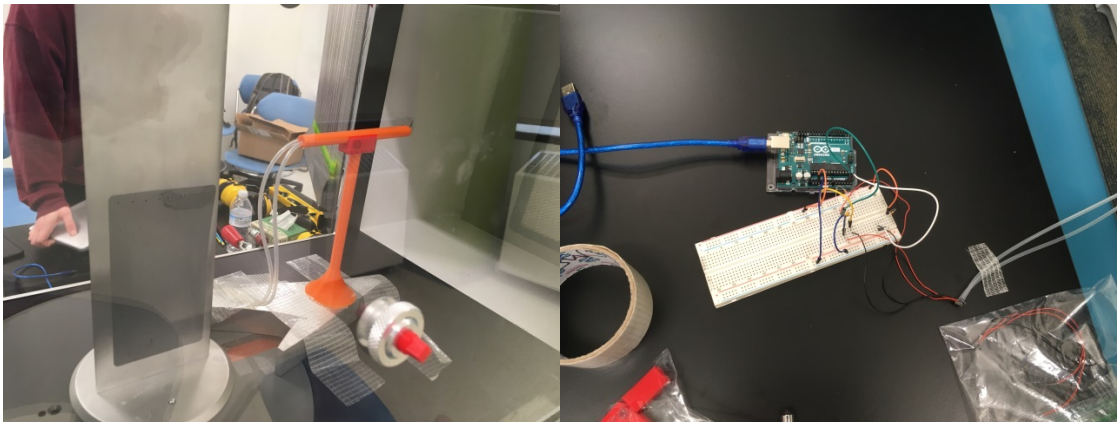

Fig. 19 (left) and 20 (right) The Beta Probe sitting on a stand within the Wind Tunnel and the Electrical Setup of the Arduino Uno and SPD31 Sensor.

Results of Wind Tunnel Tests

Roughly 4,000 data points were gathered from the wind tunnel experiments and stored in csv files. All data was imported into matlab where it was cleaned and data points at the same sideslip angle were averaged at different velocity increments. Below in figs. 21-24 are the results for slide slip angle vs differential pressure (DP) at constant velocities. Velocity data points were taken at 10, 15, 20, and 24.1m/s in figures 21-24 respectively. Side slip angle data points were taken at 7, 5, 2, 1, 0, -1, -2, -5, and -7 degrees. The zero degree sideslip angle was taken twice and the difference between data points at zero degrees deflection represents error within either the SDP31 sensor or the experimental setup. During wind tunnel testing, the SDP31 sensor was unable read pressure differentials below 8m/s, and at 10m/s, the data for beta angles between zero and two degrees were within the region of error for the sensor. Since dynamic pressure increases with the square of velocity, the differential pressure data fell outside of the range of possible sensor error at approximately 12m/s. The differential pressure data points at each velocity level fit to a linear relationship with all R^2 values equal to or above 0.99.

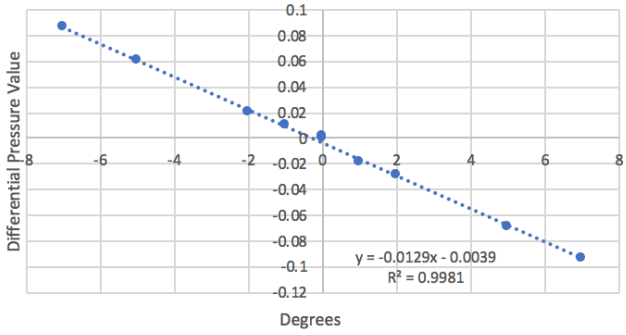

Fig. 21 Beta Angle vs. DP at 10m/s.

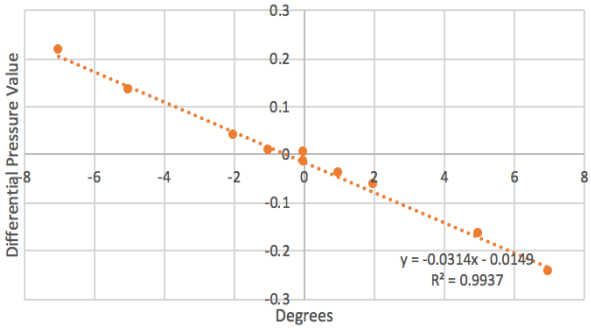

Fig. 22 Beta Angle vs. DP at 15m/s.

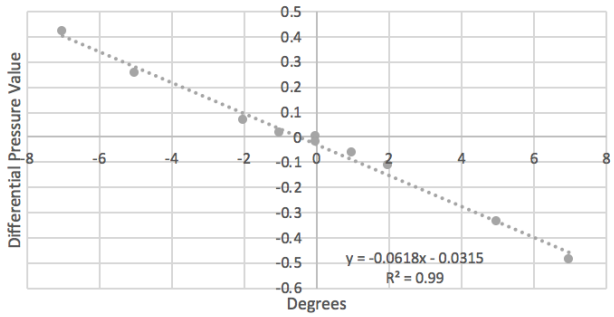

Fig. 23 Beta Angle vs. DP at 20m/s.

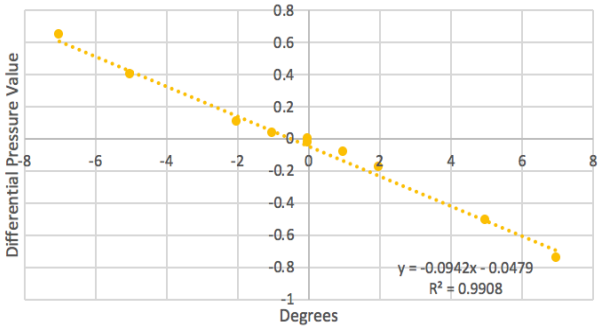

Fig. 24 Beta Angle vs. DP at 24.1m/s.

The effects of dynamic pressure on differential pressure are easily visible when the pressure plots are overlaid as shown in Fig. 25 below. The increasing distance between data points at the same deflection angle confirm a non-linear relationship dependent on dynamic pressure.

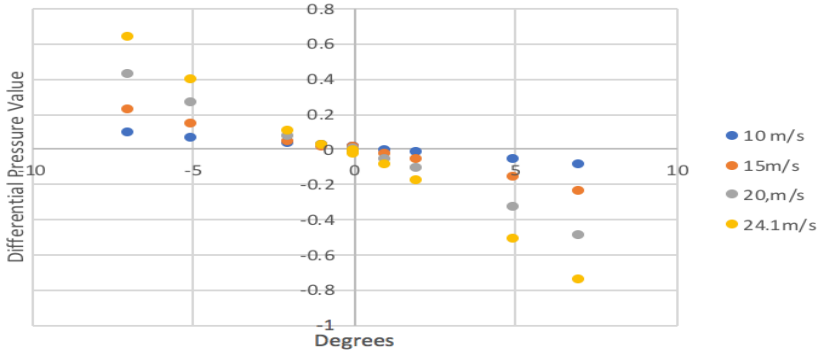

Fig. 25 Differential Pressure Values at Various Velocities and Deflections.

Beta Probe Conclusions

Despite the high R^2 value and the visible link with increasing dynamic pressure, the beta probe in its current form cannot adequately measure deflection angles at low velocities. At the most critical junctures of takeoff and landing, the beta probe is not functional as data gathered below 10m/s is within a region of possible error. This poor data precision could be the result of a dampened pressure differential. The sensor is several feet away from the probe and in that distance, the pressure wave must past through small pathways within the beta probe and approximately two and a half feet of plastic tubing. Decreasing the plastic tube length might decrease the dampening. Additionally, to directly address this issue, a more precise differential pressure sensor is required.

Acknowledgements

The financial support of the NASA Space Grant to Jonathan Richter is gratefully acknowledged. The author would like to thank Al Bowers, the former Chief Scientist of Armstrong Flight Research Center (retired), for providing a significantly improved translation of Prandtl's 1933 Paper *On Wings With The Minimum Induced Drag.* The author would also like to thank Peter Sharpe, Tejas Kelkar, and Daniel Cherenson for their help with the project.

References

[1] Anderson, J., *Fundamentals of Aerodynamics 6th Edition,* McGraw-Hill Education, New York, NY, 2017.

[2] Hainline, K., "Aerodynamic Study of Stability and Control of Flying-Wings,",2017.

[3] Bowers, A. H., and Murillo, O. J., "On Wings of the Minimum Induced Drag: Spanload Implications for Aircraft and Birds," NASA/TP-2016-219072, 2016.

[4] Prandtl, L., "Applications of Modern Hydrodynamics to Aeronautics. [in Two Parts]," National Advisory Committee for Aeronautics, 1921, pp. 157–215.

[5] Prandtl L., "Über tragflügel kleinsten induzierten widerstandes. Zeitschrift für Flugtecknik und Motorluftschiffahrt", 1 VI 1933 (München, Deustchland)

[6] Jones, R. T., "The Spanwise Distribution of Lift for Minimum Induced Drag of Wings Having a Given Lift and a Given Bending Moment," NASA Tech Note No. 2249, 1950.

[7] Klein, A., and Viswanathan, S., "Approximate Solution for Minimum induced Drag of Wings with a Given Structural Weight," AIAA Journal of Aircraft, Vol. 12, No. 2, 1975.

[8] Wroblewski, G., "Prediction and Experimental Evaluation of Planar Wing Spanloads for Minimum Drag," University of Illinois at Urbana-Champaign Thesis Paper, 2016.

[9] Iglesias, S., and Mason, W. H., "Optimum Spanloads Incorporating Wing Structural Weight," AIAA, Aircraft, Technology Integration, and Operations Forum, AIAA, Los Angeles, CA, USA, 2001. doi:10.2514/6.2001-5234.

[10] The Minimum Induced Drag of Aerofoils, NACA Report No.121,1923.

[11] A Method for Determining the Camber and Twist of a Surface to Support a Given Distribution of Lift, with Applications to the Load Over a Sweptback Wing, NACA Report No. 826, 1945.

[12] Basic Air Data, "Angle of Attack Vane", at: https://www.basicairdata.eu/knowledge-center/design/angle-of-attack-vane/

[13] Air Data Probe, Aeroprobe, at: http://www.aeroprobe.com/air-data-probe/

[14] Datasheet SDP3x-Digitial, Digital Differential Pressure Sensor, Sensiron The Sensor Company, at: https://www.sensirion.com/fileadmin/user_upload/customers/sensirion/Dokumente/0_Datasheets/Differential_Pressure/Sensirion_Differential_Pressure_Sensors_SDP3x_Digital_Datasheet.pdf

Appendix A: Beta Probe CAD Drawing